Received: 31 May 2024 | Accepted: 20 March 2025

DOI: 10.1111/1365-2478.70024

Geophysical Prospecting | EAGE EUROPEAN ASSOCIATION OF GEOSCIENTISTS & ENGINEERS

ORIGINAL ARTICLE

Seismic crosshole full-waveform inversion of high-frequency SV-waves for glacial sediment characterization

Sarah Beraus[1,2] | **Daniel Köhn**[3] | **Thomas Bohlen**[4] | **Thomas Burschil**[5] | **Bennet Schuster**[6,7,8] | **Hermann Buness**[1] | **Gerald Gabriel**[1,2]

[1]Geophysical Exploration, LIAG Institute for Applied Geophysics, Hannover, Lower Saxony, Germany

[2]Section Geology, Institute of Earth System Sciences (IESW), Leibniz University, Hannover, Lower Saxony, Germany

[3]Institute for Geosciences, Christian-Albrechts-University Kiel, Kiel, Schleswig-Holstein, Germany

[4]Geophysical Institute, Karlsruhe Institute of Technology, Karlsruhe, Baden-Württemberg, Germany

[5]B3.2, Federal Institute for Geosciences and Natural Resources, Hannover, Lower Saxony, Germany

[6]Institute of Earth and Environmental Sciences, University of Freiburg, Freiburg, Baden-Württemberg, Germany

[7]Institute of Geological Sciences, University of Bern, Bern, Switzerland

[8]Oeschger Centre for Climate Change Research, University of Bern, Bern, Switzerland

Correspondence
Sarah Beraus, Geophysical Exploration, LIAG Institute for Applied Geophysics, Stilleweg 2, 30655 Hannover, Germany.
Email: Sarah.Beraus@leibniz-liag.de

Funding information
Deutsche Forschungsgemeinschaft, Grant/Award Numbers: BU 3894/2-1, BU2467/3-1, KO6375/1-1

ABSTRACT

We present a two-dimensional, high-resolution full-waveform inversion approach of crosshole seismic data to image fine glacial sediments in an overdeepened Alpine valley, the Tannwald Basin (ICDP site 5068_1) north of Lake Constance. A vertically polarizing shear-wave source is employed to excite elastic waves, which are recorded by an eight-station three-component geophone string at 105–134 m depth. Based on traveltime tomography models derived separately from the P- and S-wave first arrival picks, we reconstruct the vertically polarized shear-wave velocity distributions from the vertical component data using isotropic, elastic full-waveform inversion. In order to mitigate the effects of source and receiver coupling, we use the global correlation norm as an objective function. The resolution is enhanced by applying an anisotropic gradient filter. The final model shows small-scale structures that look similar to a structural image obtained by seismic imaging at frequencies above 200 Hz. It provides a satisfying data fit and resolves layers of at least 1 m thickness that correlate well with the lithology derived from the core information within the errors of the source and receiver positions.

KEYWORDS
crosshole, full waveform, imaging, inversion, seismics, SV-wave

INTRODUCTION

Seismic crosshole experiments are an excellent method to obtain high-resolution subsurface models. The high-frequency sources are deployed below the weathering layer so that attenuation is significantly reduced compared to surface seismic methods. In addition, the transmission geometry can bypass surface waves and provide excellent illumination

of structures. Therefore, the crosshole method is widely used to investigate and monitor oil and gas reservoirs (Bauer et al., 2003; Rector et al., 1995; Van Schaack et al., 1995; Zhang et al., 2012), geothermal sites (Gaucher et al., 2020) and aquifers (von Ketelhodt et al., 2018).

While some studies perform reflection seismic imaging with crosshole data (Rector et al., 1995; Van Schaack et al., 1995), showing an improvement in bed thickness resolution up to 1.5 m during migration (Lazaratos et al., 1995), most authors apply inversion methods, such as traveltime tomography (e.g., Bauer et al., 2005). Rao and Wang (2005) propose methods to determine the velocity distribution in the subsurface by minimizing the ambiguity in the seismic data and the non-linearity of the inversion, using appropriate geological constraints. Von Ketelhodt et al. (2018) apply cross-gradient constraints, as formulated by Gallardo and Meju (2004), to ensure structural similarity between different parameter models when deriving geotechnical parameters of the subsurface. Further methodological assessment of seismic crosshole traveltime tomography regarding its convergence and resolution was performed by McMechan (1983) using synthetic data.

However, compared to traveltime tomography, full-waveform inversion (FWI) promises to increase the resolution to below one wavelength (Dokter et al., 2017; Köhn et al., 2019) because it takes into account all the information contained in the waveforms. It is made computationally feasible by modern high-performance computers and efficient forward solvers as well as local optimization algorithms, which mitigate the problem of higher computational cost. Comprehensive overviews of the method can be found in Plessix (2008), Buske et al. (2009), Virieux and Operto (2009) and Fichtner (2011).

FWI of crosshole seismic data has only been applied in the frequency domain (Pratt et al. (2005); Pratt & Shipp, 1999; Rao et al., 2006) due to the high source frequencies that increase the required computational resources and make time-domain applications unattractive. Wang and Rao (2006) propose strategies for real data applications of frequency-domain FWI. Bauer et al. (2005) apply acoustic frequency-domain FWI to vibro-seismic crosshole data acquired during the Mallik (2002) surveys. Synthetic studies address theoretical aspects of medium properties assumptions (acoustic/elastic/viscoelastic, isotropic/vertical transverse isotropy (VTI)/ tilted transverse isotropy (TTI)), how to incorporate geological and wireline logging data as constraints in the inversion (Singh et al., 2020, 2021) and evaluate workflows for faster convergence and better resolution. Zhou et al. (1997) showed that an elastic traveltime tomography and subsequent FWI of seismic crosshole data can improve the resolution from 20 m in traditional reflection seismic processing to 3 m for the P-waves and 1.5 m for the S-wave. Hadden et al. (2019) show that a quarter wavelength vertical resolution can be achieved by an anisotropic frequency-domain FWI when a Gaussian smoothing filter is applied to the gradients, effectively pushing the medium towards one dimension. Time-domain FWI field application of surface seismic data often uses SH-waves (Mecking et al., 2021) and surface waves (Gao et al., 2023) to image the near surface, since S-waves provide a factor of 2–10 better resolution than P-waves according to Stümpel et al. (1984).

Here, we present an innovative field data application of conventional FWI, where we investigate the suitability and resolution capability of high-frequency vertically polarized shear waves that are excited by a novel borehole source for imaging finely layered glacial sediments in the overdeepened Alpine Tannwald Basin (Germany) with elastic isotropic, time-domain FWI (Köhn et al., 2012) in a crosshole setting with a little parameter tuning or most advanced regularization tools.

FULL-WAVEFORM INVERSION METHODOLOGY

In order to obtain high-resolution subsurface images of the glacial sediments, we choose full-waveform inversion (FWI) because the method does not only take into account the phase information of the seismic waves but also their amplitude. This allows us to push the resolution below the dominant seismic wavelength (Virieux & Operto, 2009). In this study, we focus on the inversion of the vertical component of the SV-wave data and use the open-source software DENISE-Black-Edition which is available at https://github.com/daniel-koehn/DENISE-Black-Edition.

Two-dimensional coupled P- and SV-wave elastic equations of motion

A crucial part of the FWI approach is the accurate forward modelling of the seismic wavefield. Here, we apply time-domain finite-difference (FD) modelling on a staggered grid to numerically solve the 2D isotropic elastic equations of motion for the coupled P- and SV-wave propagation (P-SV case) (Levander, 1988; Virieux, 1984). The equations are given in the stress–velocity formulation in the form of a system of first-order partial differential equations as

$$\begin{aligned}\rho\frac{\partial v_x}{\partial t} &= \frac{\partial \sigma_{xx}}{\partial x} + \frac{\partial \sigma_{xz}}{\partial z}\\ \rho\frac{\partial v_z}{\partial t} &= \frac{\partial \sigma_{xz}}{\partial x} + \frac{\partial \sigma_{zz}}{\partial z} + f_z\\ \frac{\partial \sigma_{xx}}{\partial t} &= (\lambda+2\mu)\frac{\partial v_x}{\partial x} + \lambda\frac{\partial v_z}{\partial z}\end{aligned} \tag{1}$$

$$\frac{\partial \sigma_{zz}}{\partial t} = \lambda \frac{\partial v_x}{\partial x} + (\lambda + 2\mu) \frac{\partial v_z}{\partial z}$$
$$\frac{\partial \sigma_{xz}}{\partial t} = \mu \left(\frac{\partial v_x}{\partial z} + \frac{\partial v_z}{\partial x} \right),$$

where x and z are the horizontal and vertical coordinates, respectively, while t is the time, ρ is the density and λ and μ are the Lamé parameters. The particle velocities are denoted as v_i and the stress components as σ_{ij}, where the indices indicate their respective directions; f_z represents the vertical force source term.

Two-dimensional vertically polarized S-wave full-waveform inversion

FWI aims to find the optimum model that best explains the observed wavefield by minimizing the misfit between the field and the modelled data in an iterative approach. Starting with an initial model $\mathbf{m}_0$, the model parameters are updated at each inversion step n along a search direction $\delta \mathbf{m}_n$ by

$$\mathbf{m}_{n+1} = \mathbf{m}_n + \alpha_n \, \delta \mathbf{m}_n, \tag{2}$$

where α_n is the step length determined in a parabolic line search to ensure proper convergence (Nocedal & Wright, 2006). The model update at inversion step n is defined by

$$\delta \mathbf{m}_n = -\mathbf{H}_n^{-1} \left(\frac{\partial E}{\partial \mathbf{m}} \right)_n \tag{3}$$

with the inverse Hessian matrix $\mathbf{H}^{-1}$ and the gradient of the misfit $\partial E / \partial \mathbf{m}$. The latter is calculated with the adjoint-state method using the stress–velocity parameterization (Köhn et al., 2012; Tarantola, 2005). The product of inverse Hessian and misfit gradient is approximated by a quasi-Newton l-BFGS (limited-memory Broyden–Fletcher–Goldfarb–Shanno algorithm) approach (Métivier & Brossier, 2016; Nocedal & Wright, 2006). Further details on the FWI strategy and the definition of the misfit function E are given in the Full-Waveform Inversion strategy subsection 4.5.

GEOLOGY

Overdeepened valleys

Overdeepened valleys are elongated structures that were excavated from the bedrock by a glacier below the fluvial base level and later refilled, often in several cycles, by rocks and sediments transported by the glacial system (Cook & Swift, 2012). While the formation process of overdeepening is still under debate, the buried landforms are undoubtedly valuable climate archives in currently and formerly glaciated regions (Gegg & Preusser, 2023). In the northern Alps, their formation is also governed by local topography and geology and, thus, by the Alpine orogeny, where the collision of the African continent with the European yields the formation of the wedge-shaped North Alpine Molasse Basin (Pfiffner, 1986). This process significantly influenced the flow of rivers in the region and thus erosion and sedimentation processes. Preusser et al. (2010) and Ellwanger et al. (2011) link the formation of such overdeepened structures in the Alps to climate changes in the Middle to Late Pleistocene and argue that overdeepening can also be found in the Alpine foreland.

Study site: Tannwald Basin (ICDP site 5068_1)

After the Alpine Rhine took its current course in the Early Pleistocene (Ellwanger et al., 2003; Pfiffner, 2014), at least two glacial cycles formed the overdeepened north-south trending Tannwald Basin in the Quaternary (Ellwanger et al., 2011; Preusser et al., 2010). During the Hosskirch glaciation, a Rhine Glacier lobe incised into the bedrock of Tertiary Upper Freshwater Molasse and the underlying Upper Marine Molasse at the basin's deepest part forming the D3 discontinuity (Ellwanger et al., 2011), which is indicated in Figure 1. Today, the Tannwald Basin forms an approximately 1 km wide and up to 250 m deep, distal overdeepened structure. Its infill consists of waterlain till and molasse slabs, which were deposited during the Hosskirch glaciation and appear as strong, seismic reflectors (Burschil et al., 2018). These are followed by basinal, fine-grained sediments that accumulated as laminated fines in the large glacial lake until the Early Rissian. Above this, the change to coarse-grained clastics intercalated with till layers, known as the D2 discontinuity (Figure 1), marks the advance of a glacier lobe during the Riss glaciation. The uppermost layer is made up of glaciofluvial gravels of the outwash plain of the Last Glacial Maximum (LGM) with a thickness of about 10 m (Buness et al., 2022) and indicates another glacial advance.

Our study site (ICDP site 5068_1) is located about 45 km north of Lake Constance, just beyond the terminal moraine of the LGM (Figure 1) so that the D1 discontinuity does not occur. At the site, three boreholes were drilled down to the bedrock at about 160 m depth. Two of those are flush drillings (A and B), and C is a cored drilling (Figure 2). The boreholes are arranged in an isosceles triangle with its edges of 28 m length oriented in north-south and west-east directions. Recently, Schuster et al. (2024) derived seven lithofacies assemblages based on sedimentary characteristics found in the core and related them to the glacial history of the overdeepened valley.

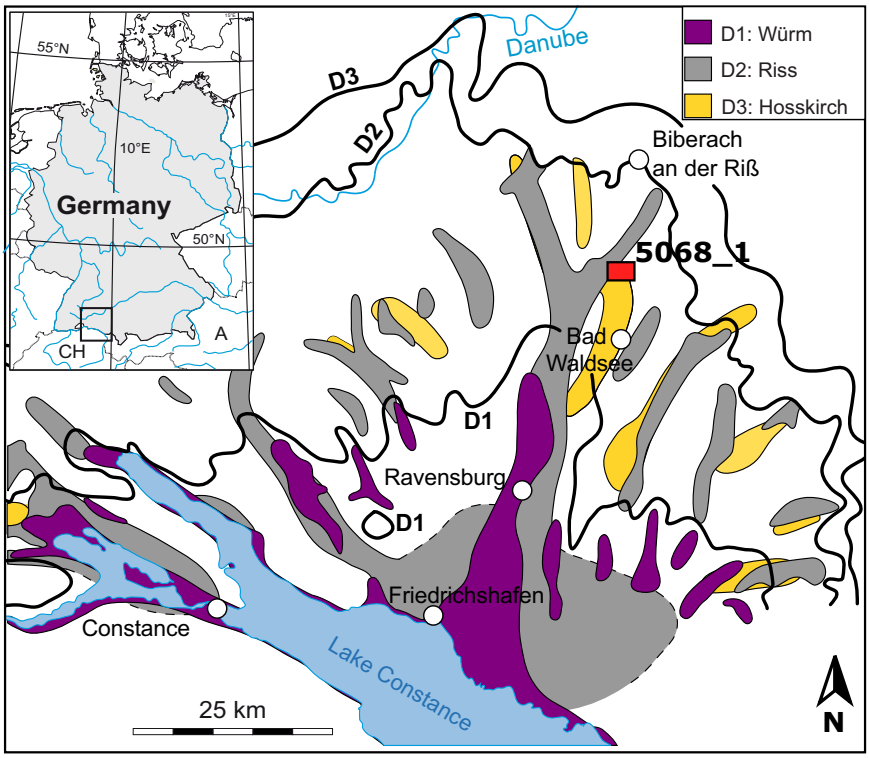

FIGURE 1 Map of the overdeepenings of the Rhine Glacier in the Quaternary in the northern Alpine Foreland (modified after Ellwanger et al., 2011, and Beraus et al., 2024). The study site is marked by the red square. Black lines indicate the maximum ice extent during the corresponding glaciation period.

DATA ACQUISITION AND PRE-PROCESSING

Vertically polarized S-wave crosshole data acquisition

The SV-crosshole experiment was one of three crosshole experiments conducted at the ICDP DOVE Tannwald site (5068_1) in 2022. The transmission geometry has the advantage of illuminating the subsurface densely and circumventing the dampening weathering layer, thus, preserving the high-frequency information. The target zone of the SV-acquisition was the finely layered sediments at about 105–134 m depth, which were identified based on preliminary information from cuttings of the flush drilling B and core catcher data of the core drilling C, since the final detailed analyses have not yet been available when the experiment was conducted. The vertically polarizing shear wave borehole source, which was pneumatically clamped to the borehole wall, was excited four times every meter from 77 to 143 m depth in borehole B. In order to record the wavefield, we chose a sampling frequency of 8 kHz and placed an eight-station three-component (3C) 10 Hz eigenfrequency geophone string with a receiver spacing of 2 m at depths from 105 to 134 m in borehole C. The receiver spacing was reduced to 1 m and a reasonable depth coverage was achieved by shifting the receiver string three times, making sure that the two deeper receiver layouts overlapped with the two shallower receiver layouts at one station.

Pre-processing

After assigning the geometry, vertically stacking the repeated shots and picking P- and S-wave first arrivals, we tested several zero-phase bandpass filters to ascertain the frequency content of the data. The cumulative power spectrum of the dataset (grey), the cumulative spectrum of the *Z*-component (black) and the power spectra of three selected shot gathers (coloured) are shown in Figure 3. We identify the frequency contribution below 80 Hz as noise. Frequencies between 80 and 650 Hz predominantly make up the S-wave. Higher frequencies represent the P-wave (peak frequency ~1200 Hz; not shown here) and short-period noise.

In preparation for FWI, we mute the trigger peak at time zero. We then apply a 3D-to-2D spreading correction (Bleistein, 1986), since the measured 3D wavefield and the simulated 2D wavefield differ in amplitude and phase (Forbriger et al., 2014; Schäfer et al., 2014). Afterwards, we test the source-time function (STF) inversion including all offsets to determine the required damping parameter of the stabilized Wiener deconvolution, that is applied in the frequency domain, to 1%. During these tests, we also find that a time delay of 0.1 s is required to obtain a causal source wavelet. Finally, we apply a shot-wise normalization to the absolute maximum amplitude which reduces the influence of the source and receiver coupling on the amplitudes (Schwardt et al., 2020). Figure 4 depicts the results of the pre-processing of the vertical *Z*-component for the shallowest, the intermediate depth and the deepest shot.

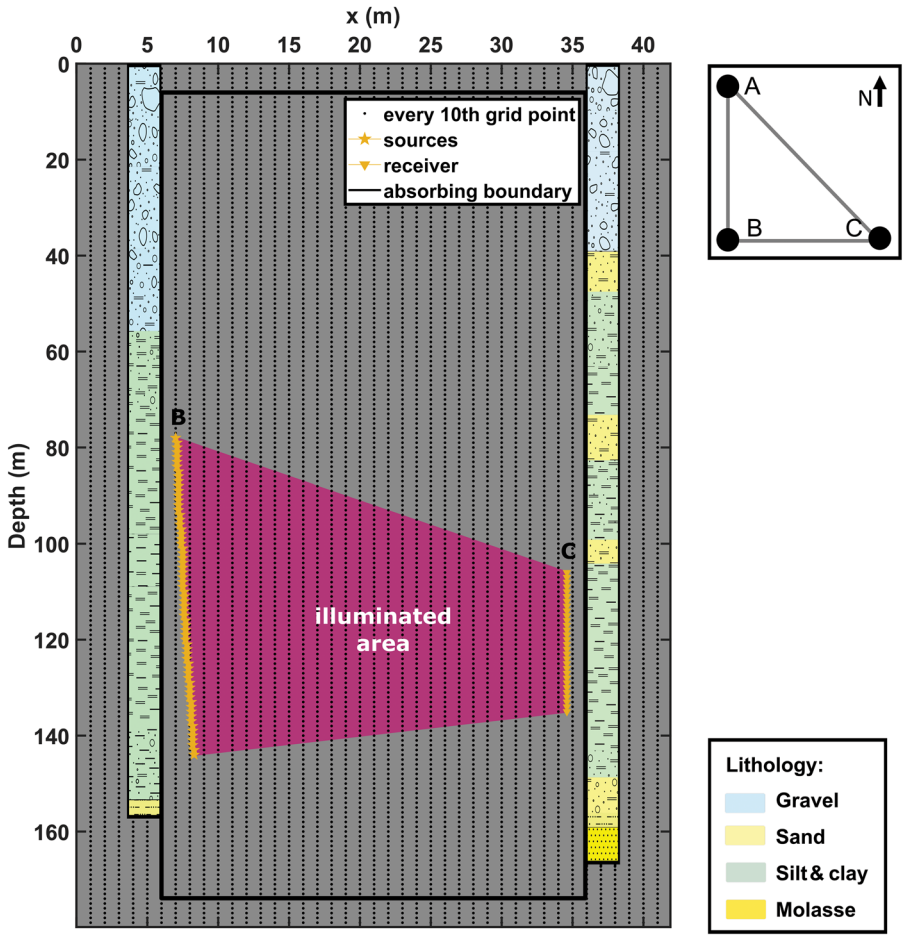

FIGURE 2 SV-survey coverage between boreholes B and C and preliminary lithology of the flush drilling B and the cored drilling C. The geographical orientation of the boreholes is shown in the map view in the top right corner. The source was placed in borehole B, and the eight-station 3C geophone string was placed in borehole C. Preliminary lithological information was derived from cuttings (B) and core catcher (C) information during drilling. Sand layers in borehole B cannot be identified due to mixing with the drilling mud. The survey coverage is based on a straight ray assumption and is coloured in pink. Additionally, every tenth grid point of the FD grid and the boundary of the absorbing frame are shown by the black dots and bold lines, respectively. Please note that the figure is exaggerated by about a factor of four in the horizontal x-direction. The borehole trajectory was projected onto the 2D modelling plane in an offset-consistent manner.

Initial model building

To obtain initial models for FWI, we use the P- and S-wave first arrivals and perform separate traveltime tomographies using the damped Gauss–Newton algorithm with global (Günther et al., 2006) and additional geostatistical regularization (Jordi et al., 2018) using the inversion code *pyGIMLi* (Rücker et al., 2017). The specific inversion parameters are listed in Table A.1 in the Appendix. The traveltime inversions of P- and S-wave picks yield structurally different models. We assume that density changes in the considered depth range mainly result from the compaction of the sediments allowing to use a linear relationship with the SV-wave velocity (in m s^{-1}) given by

$$\rho = 1600\ \text{kg m}^{-3}\left(1+\frac{v_{\text{SV}}}{1600\ \text{m s}^{-1}}\right), \tag{4}$$

and which was applied to a burial mound consisting of fluvial sediments by Mecking et al. (2021) using the SH-wave velocity. The resulting density value of 2190 kg m^{-3} lies in the range of values from the open-hole logging information available at borehole C.

The S-wave tomography model implies earlier S-wave arrivals than observed in the field data. Therefore, we reduce the S-wave velocity by 5% such that the S-wave arrivals are fit by the wavefield simulation. The final tomography models and the density model, which is once again calculated from v_{SV}, are shown in Figure 5. The most significant features are the high-velocity layer below 140 m depth, the low-velocity zone in about 115–140 m depth in the east as well as the depression in the centre of the S-wave model.

The models are discretized on a Cartesian staggered grid with a grid spacing of 0.1 m to avoid numerical dispersion when using a sixth-order finite-difference (FD) operator in

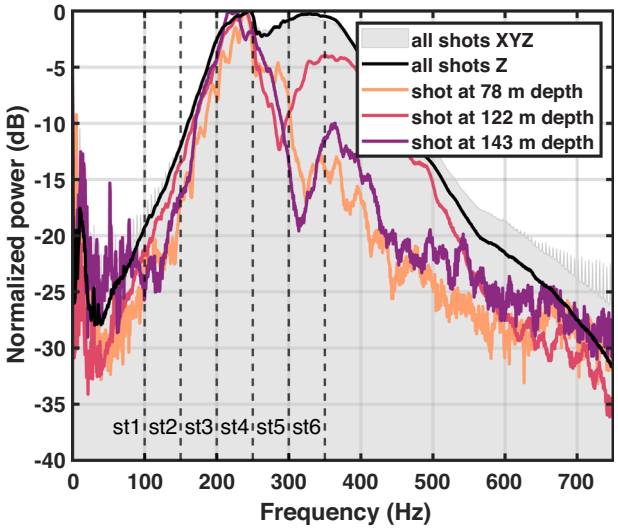

FIGURE 3 Cumulative power spectrum of the data that was acquired with an SV-source in borehole B and an eight-station 3C geophone string in borehole C (grey) and *Z*-component only (black). The significant contributions below 80 Hz are related to noise and barely contain any signal. The coloured curves refer to the *Z*-component of the shot gathers presented in Figure 4. The upper bounds of the frequency stages that are used in the FWI are marked by vertical black dashed lines and are labelled by 'st1' to 'st6', denoting stages 1 to 6, respectively.

space with Taylor coefficients (Figure 2) (Dablain, 1986; Levander, 1988). We also add about 3 m thick model boundaries on each side of the model to absorb artificial reflections at the model boundaries using an absorbing boundary zone in the form of a convolutional perfectly matched layer (Komatitsch & Martin, 2007). This results in an FD grid of 1800×420 ($NZ \times NX$) grid points.

Forward modelling

To test the suitability of our models for FWI, which uses a local optimization approach, we forward model the wavefield based on these models using a lowpass-filtered spike wavelet ($f \leq 325$ Hz) together with a vertical force source mechanism, and apply the STF inversion to the data which is bandpass filtered to a frequency range of 80–250 Hz and 80-350 Hz, respectively, to show the waveform fit. To fulfil the Courant–Friedrichs–Lewy stability criterion (Courant et al., 1967), we choose a temporal discretization of 0.01 ms with a second-order FD operator in time. Figures 6 and 7 that the simulated data already fit the observed data within half a period on most traces, neglecting the amplitude misfit. Thus, the tomography models might be sufficient to be used as starting models in FWI with our dense transmission geometry. We propose to mitigate the remaining misfit by our FWI strategy (see the next subsection 4.5) to avoid cycle skipping and ultimately ensure proper convergence of the inversion.

TABLE 1 FWI workflows. Six frequency stages are used starting at 80 Hz. During stages 1–3 an isotropic Gaussian gradient filter ($\gamma_x = \gamma_z$) is applied, which is defined by the horizontal and vertical correlation lengths γ_x and γ_z, respectively. Stages 4–6 use an anisotropic gradient filter ($\gamma_x > \gamma_z$).

Stage	$f_{\min}$ (Hz)	$f_{\max}$ (Hz)	γ_x	γ_z
1	80	100	2.5	2.5
2	80	150	2.0	2.0
3	80	200	1.5	1.5
4	80	250	2.5	0.5
5	80	300	2.5	0.5
6	80	350	2.5	0.5

Full-waveform inversion strategy

In this study, we focus on the inversion of the S-wave velocity from the vertical component of the SV dataset, where we keep the P-wave velocity and density constant. Due to the inversion problem being highly non-linear, we apply the multi-stage approach (Bunks et al., 1995; Groos et al., 2017) as given in Table 1, where we filter the data at each inversion stage with a sixth-order zero-phase bandpass filter with a lower corner frequency of 80 Hz (see Table 1), apply the STF inversion at the first iteration of each new frequency stage and run at least 20 iterations per frequency stage. In addition, the choice of objective function is very important. Since we expect large amplitude variations caused by source and receiver coupling effects, we choose the global correlation norm (GCN) given by

$$E = -\sum_{i=1}^{ns} \int_0^T \mathrm{d}t \sum_{j=1}^{nr} \left[\frac{u_{ij}^{\mathrm{mod}}(t)\, u_{ij}^{\mathrm{obs}}(t)}{\|u_{ij}^{\mathrm{mod}}(t)\|_2 \, \|u_{ij}^{\mathrm{obs}}(t)\|_2} \right], \qquad (5)$$

where *ns* and *nr* are the number of sources and receivers and T is the recording time. The modelled and observed data are denoted as u_{ij}^{mod} and u_{ij}^{obs}, respectively, and $\|\cdot\|_2$ is their L2-norm. The GCN objective function uses the traces normalized to the absolute maximum amplitude, thus reducing the sensitivity to amplitude errors and effectively giving the phase information a higher weight (Choi & Alkhalifah, 2012; Dokter et al., 2017; Schwardt et al., 2020). In order to reduce the memory required for the inversion, we apply a quasi-Newton l-BFGS algorithm for optimization, where we save only 20 of the most recent gradients. Furthermore, we approximate the initial guess of the inverse Hessian matrix by the squared absolute value of the forward wavefield (Zhang et al., 2012).

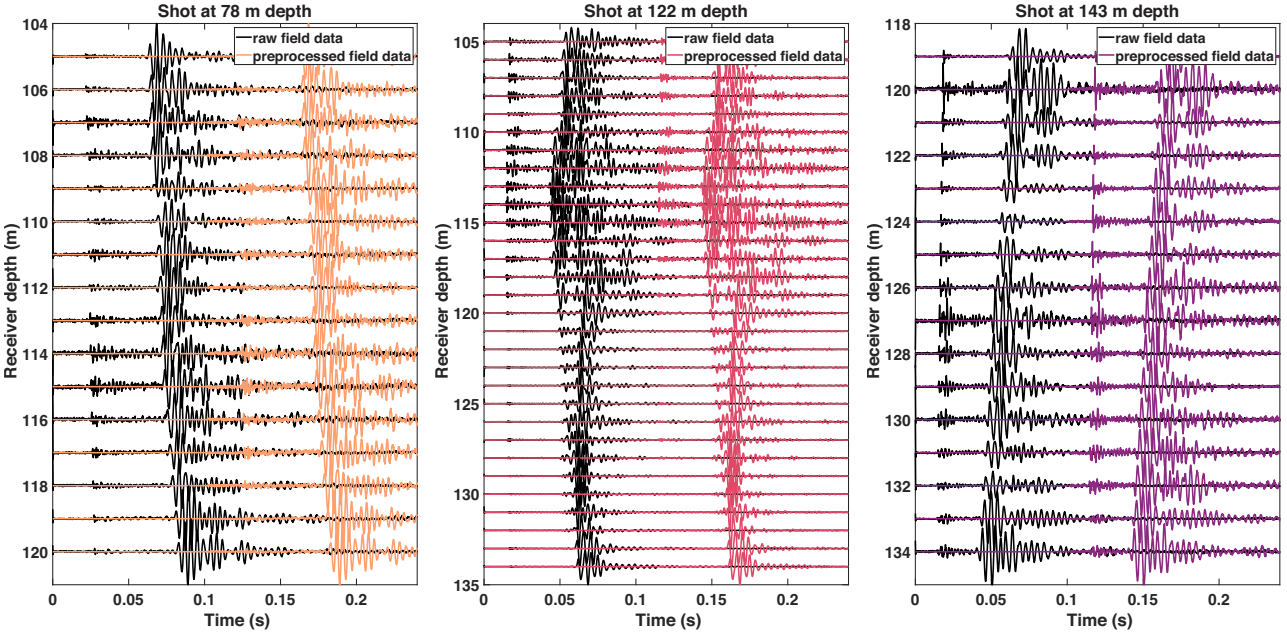

FIGURE 4 Comparison of the raw and the pre-processed field data with the full frequency content (0–4000 Hz).

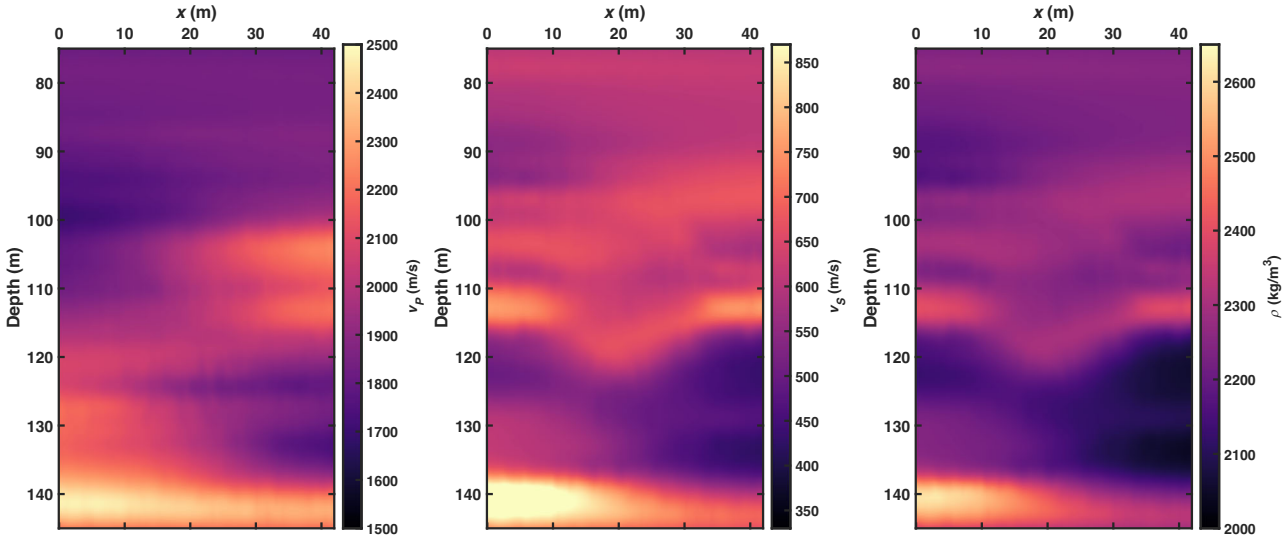

FIGURE 5 Traveltime tomography models and density model. The S-wave model (centre) clearly shows structural differences compared with the P-wave model (left). The density is calculated based on the S-wave velocities.

Gradients of the objective function with respect to the material parameters are calculated in the time domain by performing a zero-lag cross-correlation between the forward modelled and the adjoint wavefields, which must be stored in the RAM. To save RAM, we make use of a strict Nyquist criterion formulated by Kurzmann (2012) as

$$DT_{\text{samp}} \leq \frac{1}{8\, f_{\max}}, \tag{6}$$

where $f_{\max}$ is the maximum frequency at the current inversion stage and DT_{samp} is the time sampling interval at which the wavefield has to be saved to accurately apply the imaging condition while reducing the number of stored wavefields.

We smooth the gradient using a Gaussian filter to remove short wavelength artefacts (Ravaut et al., 2004). The filter is defined relative to a fraction of the minimum S-wave wavelength, denoted as γ_S. In the first three inversion stages, that is, up to 200 Hz, we decrease γ_S from 2.5 to 1.5 in steps of

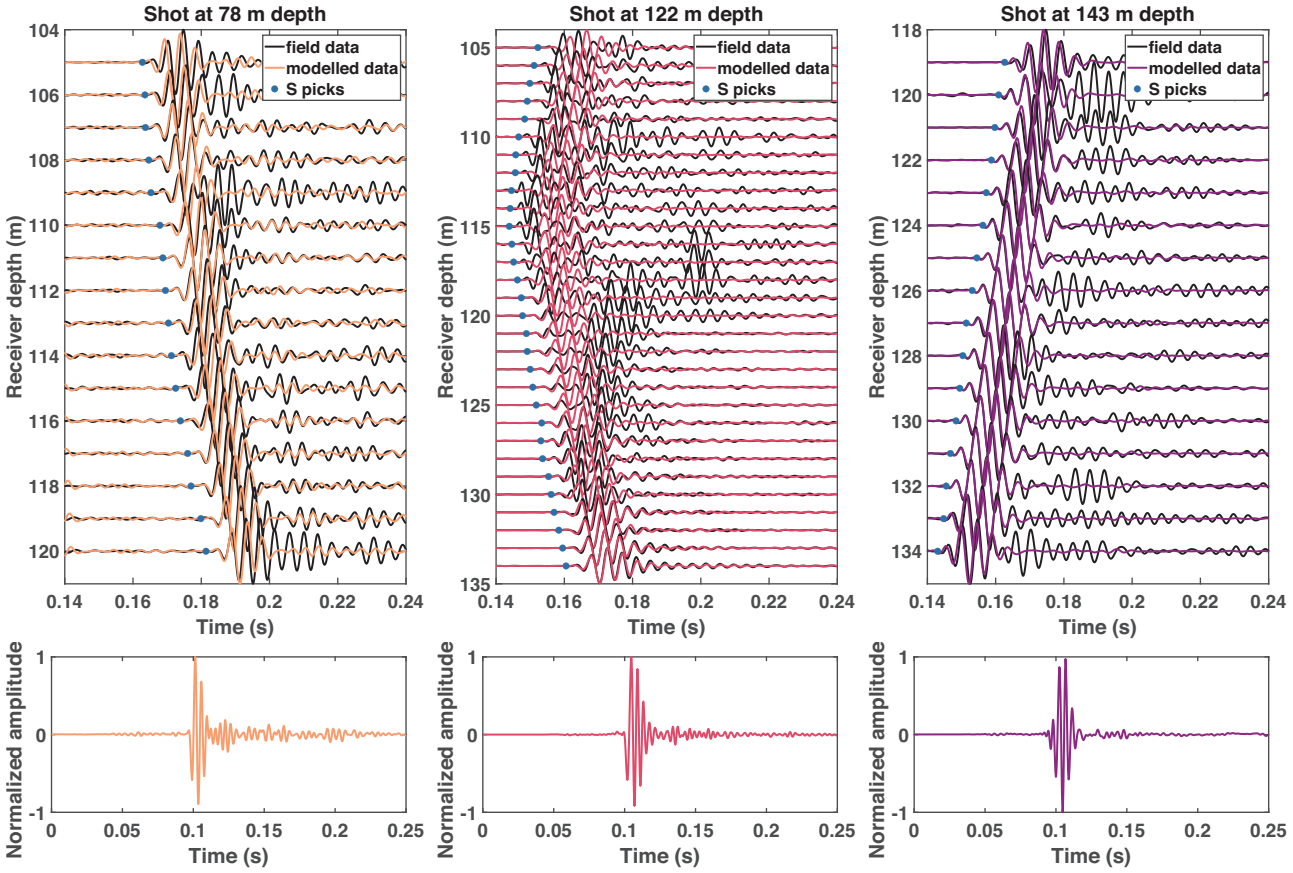

FIGURE 6 Top: Comparison of forward modelled data based on the traveltime tomography models including STF inversion and the pre-processed and bandpass filtered (80–250 Hz) field data. The data misfit is smaller than half a period for most shots and traces. Bottom: Normalized wavelets obtained by STF inversion using the stabilized Wiener deconvolution.

0.5 at every inversion stage effectively using isotropic gradient filters. At higher frequencies, however, we increase the horizontal correlation length (γ_x) to the same fraction as in stage 1, but further decrease the vertical correlation length (γ_z) (see Table 1). Thus, we make the filter anisotropic, which improves the vertical resolution for the cost of a loss in the horizontal resolution of less than 0.2 m. In addition, we apply a cylindrical taper at each shot position.

FWI aborts if one of the abort criteria is reached. We define them as (a) a relative misfit change of less than 1%, (b) a failed line search after six attempts and (c) a maximum number of total iterations of 600.

RESULTS

Field data full-waveform inversion results

The FWI results at frequency stages 4 and 6 are presented in Figure 8. The inversion predominantly updates the starting model in the regions expected based on the source–receiver geometry and enhances the velocity contrasts. Significant features are the two high-velocity layers at about 106 (a) and 138 m depth (f), which extend west to east across the velocity model. At around 113 m depth, we see a high-velocity zone near the receiver borehole C in the east (b), accompanied by a small low-velocity zone just above it. At about 120 m depth (c), the depression from the tomography models is now slightly smeared at the source side. Below this, we observe a low-velocity zone, followed by a bending layer of higher velocity (d), and in the deep eastern part a zone of low velocity with more internal layered structures (e).

The FWI converges at stage 6 after 127 iterations, achieving a relative misfit reduction of up to about 17% in the first two frequency stages, as illustrated in Figure 9. From stage 3 onward, the misfit changes are minor. The absolute, normalized misfit at the beginning of each frequency stage is greater than the initial one. The stage 4 model shown in Figure 8 (top), which is inverted at iteration 85, reveals that the main structures of the starting model remain intact, while smaller structures, such as the fine layering observed in region (e), emerge. These structures are further enhanced in the higher frequency stages (Figure 8 (bottom)). Figure 10 shows the waveform fit after stage 4 of the inversion. The synthetic data

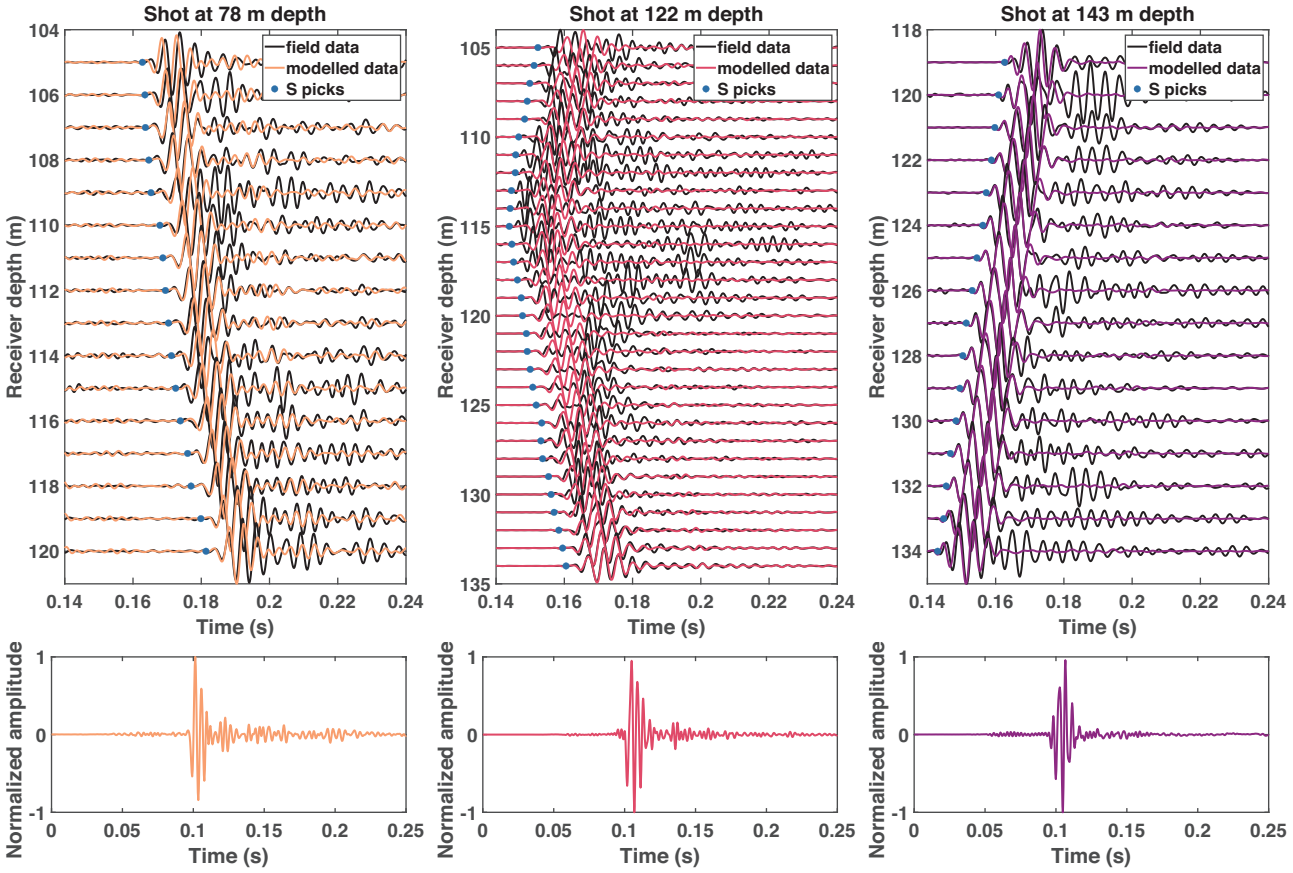

FIGURE 7 Top: Comparison of forward modelled data based on the traveltime tomography models including STF inversion and the pre-processed and bandpass filtered (80–350 Hz) field data. The data misfit is smaller than half a period for most shots and traces. Bottom: Normalized wavelets obtained by STF inversion using the stabilized Wiener deconvolution.

fit the field data very well at the shallowest shot at 78 m depth and the deepest shot at a depth of 143 m. However, some amplitude differences are observed for later arrivals. For the intermediate shot at 122 m depth, the inversion correctly predicts the first S-wave arrival at all receivers. Nevertheless, the amplitude discrepancies remain for the early S-phases at intermediate depths of 120–127 m, where a linear event is observed. The waveform fit at stage 6 (Figure 11 (bottom)) is similar, though in comparison, later arrivals match better, while the coda of the earlier arrivals is fitted slightly worse.

The waveform fit is also reflected by the inverted source wavelets (Figures 10 (bottom) and 11 (bottom)), which mostly have a sharp onset and a longer coda than at the initial fit (Figure 6 and 7).

Synthetic resolution test

To investigate the resolution capacity of the data and the FWI approach as well as possible numerical artefacts, we perform two resolution tests. The first test targets the resolution capability of thin layers using the one-dimensional model shown in Figure 12 (left). The model is obtained by horizontally smoothing the stage 4 FWI result using a homogeneous starting model. We create synthetics by forward modelling the elastic wavefield using the low-pass filtered spike wavelet. Afterwards, we invert these data using a homogeneous starting model of 590 m/s and the same FWI strategy as for the field data.

Figure 12 (centre) shows the results at stage 4 (top) and stage 6 (bottom). In the regions that are traversed by the directly transmitted waves, the layers are reconstructed, outside not. At the receiver side in the east, the reconstruction is better than on the source side, that is, thinner layers can be distinguished. The deepest layers are slightly concave. The maximum absolute difference between the original and the inverted model at stage 4 is less than $\pm 65\ \mathrm{m}^{-1}$, corresponding to approximately 11%. At stage 6, this is reduced further but not significantly. The resolution test does not show kernel-shaped or slightly bent, fine-scale structures in the reconstructed models or the difference plots (Figure 12, right) proving the fine structures are not numerical.

The second test investigates how well quadratic anomalies with a side length of 1.2 m ($\sim 0.55\,\lambda_{\mathrm{mean}}$ or $\sim \lambda_{\mathrm{min}}$ in

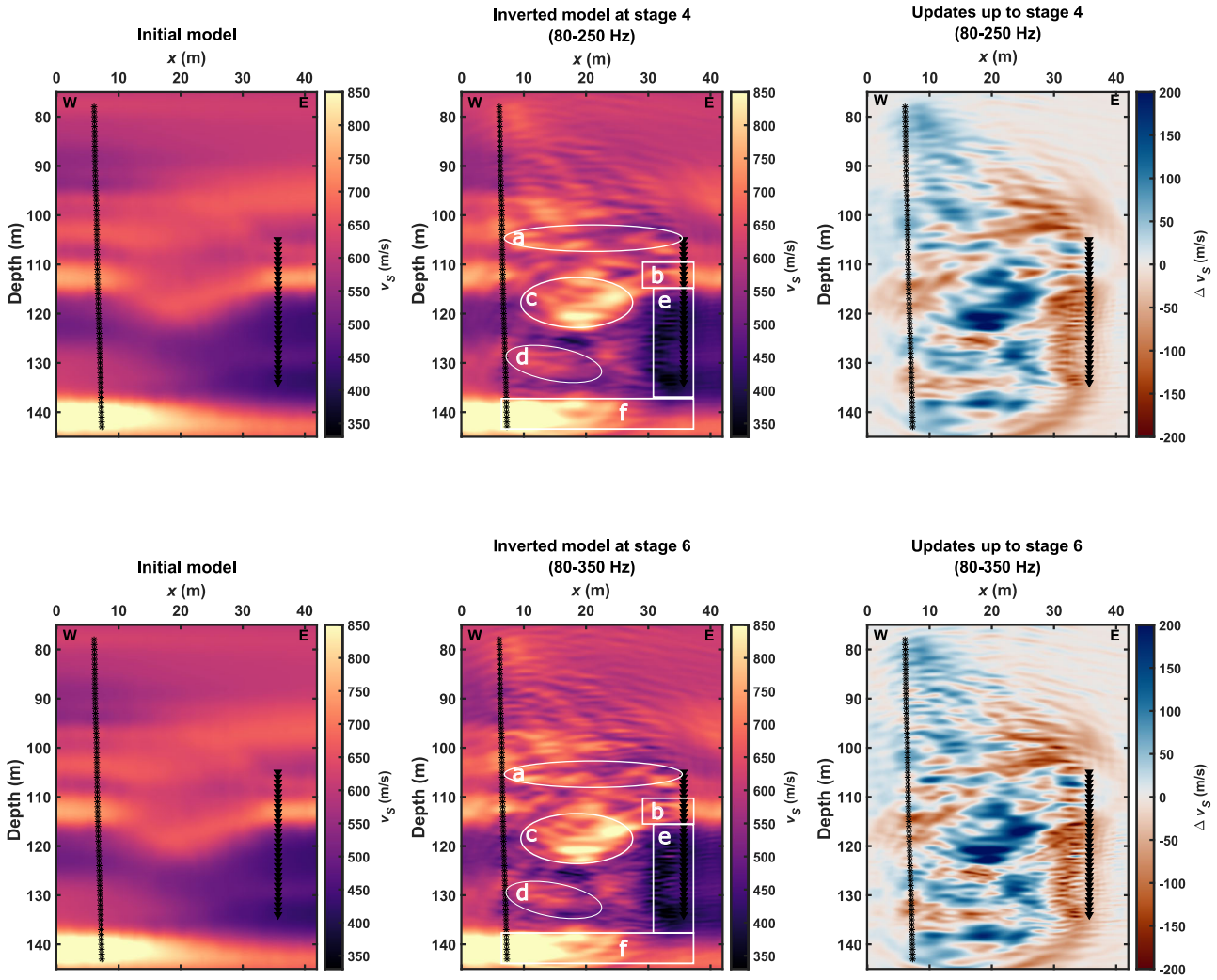

FIGURE 8 Left: Traveltime tomography model, centre: FWI result at stage 4 (top) and stage 6 (bottom), and right: the difference between the initial and inverted model at stage 4 (top) and stage 6 (bottom). Source positions are marked by stars (*) and receiver positions are marked by triangles (▼). The marked structures are introduced in subsection 5.1 and explained in subsection 5.3.

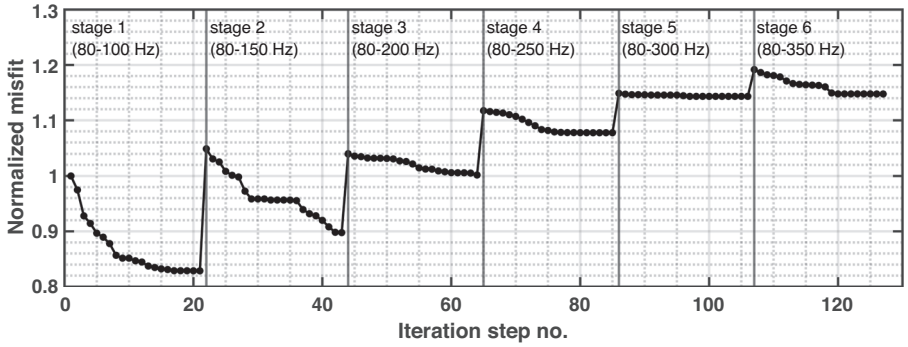

FIGURE 9 Misfit evolution during the FWI normalized to initial misfit. The frequency content of the inversion stages is provided, and the first iteration step at the new stages is marked by vertical lines.

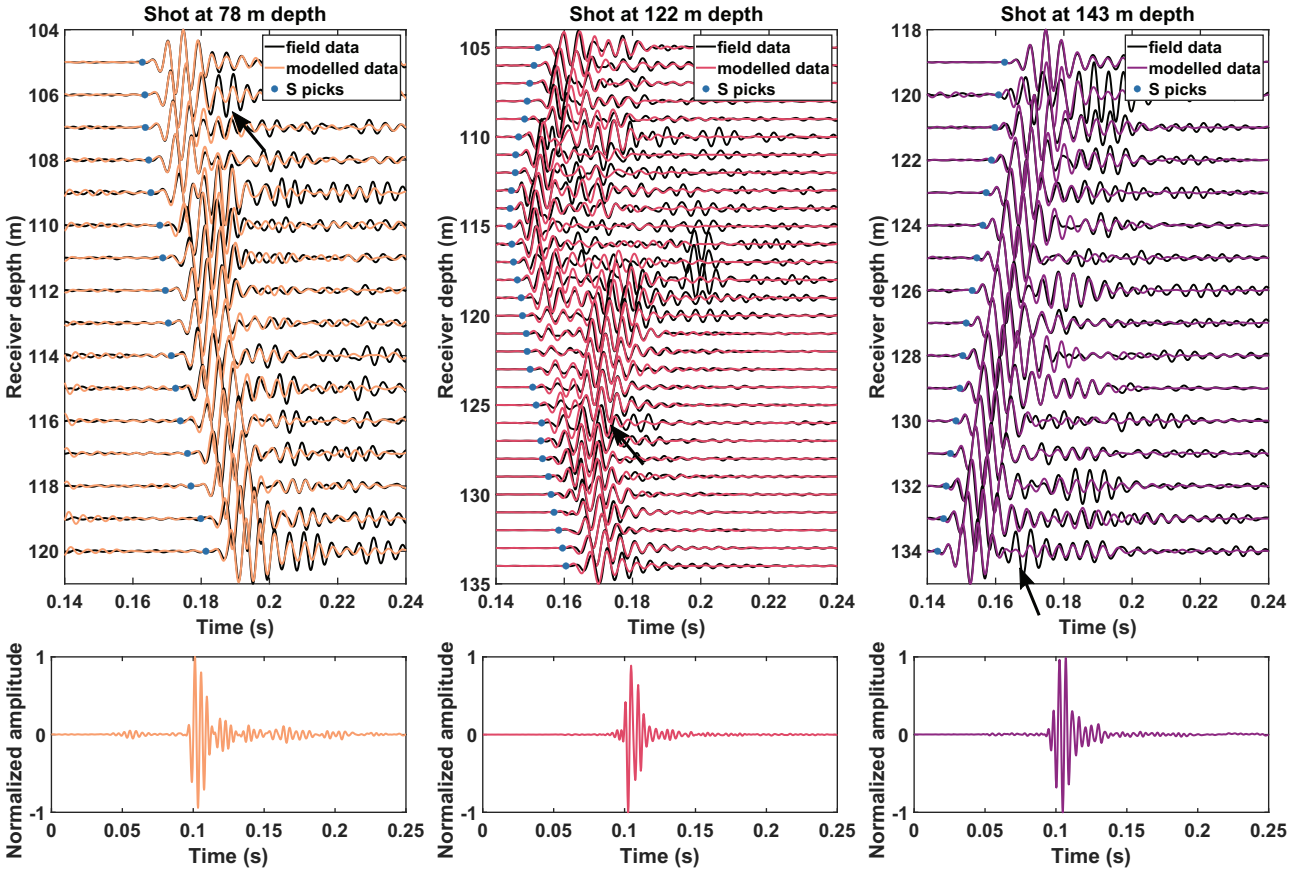

FIGURE 10 Top: SV-waveform fit for the model at stage 4 (80–250 Hz) of the FWI (Figure 8 (top)) with the traveltime tomography models in Figure 5 used as starting models. The arrows mark where we observed a better fit at stage 4 than at stage 6. Bottom: Normalized wavelets obtained by STF inversion using the stabilized Wiener deconvolution.

the tomography model at the peak frequency of 350 Hz) can be resolved in a background model given by the traveltime tomography model and thereby test the lateral resolution of the FWI strategy. The low- and high-velocity anomalies have velocities of 450 and 750 m/s, respectively (Figure 13, left). We forward model the elastic wavefield using the low-pass filtered spike wavelet and invert the synthetic data using the same FWI strategy as for the field data, with the exception of the STF inversion.

Figure 13 (centre) shows the results at stage 4 (top) and stage 6 (bottom) and Figure 13 (right) the difference between the initial model and the FWI models. As expected, solely the region covered by the source–receiver geometry is updated. The central anomaly at the top is significantly smeared in the direction of the expected ray paths. Similarly, the bottom row anomalies only yield concave artefacts in the difference plots. It can be observed that most anomalies exhibiting a significant velocity contrast relative to the background model are recovered well. One example is the low-velocity anomaly just above 130 m depth on the receiver side. While the upper and lower edges are sharply reconstructed, the anomalies are smeared horizontally, which makes them up to four times as wide as they actually are corresponding to about the length of the gradient smoothing operator. Additionally, weak artefacts are introduced into the model above and below the well-reconstructed anomalies, and some diagonal smearing occurs, for instance, at the central anomaly at 105 m depth.

Interpretation

To better assess the quality of the FWI and to ground-truth it, we compare the velocity profile extracted along borehole C from the FWI at stage 4 with the lithology derived from core information by Schuster et al. (2024) (Figure 14). At shallow receiver depths of 105–110 m, where massive and laminated fines (Fm, Fl) as well as massive and laminated sand layers (Sm, Sl) are present, mainly long-period trends correlate. In the fines representing rhythmites with occasional dropstones (Flr, Flr(d)) found in the deeper half (Schuster et al., 2024), even the thin layers can be distinguished in the SV-wave velocity profiles at about 120 m depth. The diamict layers at 137.2–138.8 m and 143.6–146.8 m depth, however, cannot be correlated.

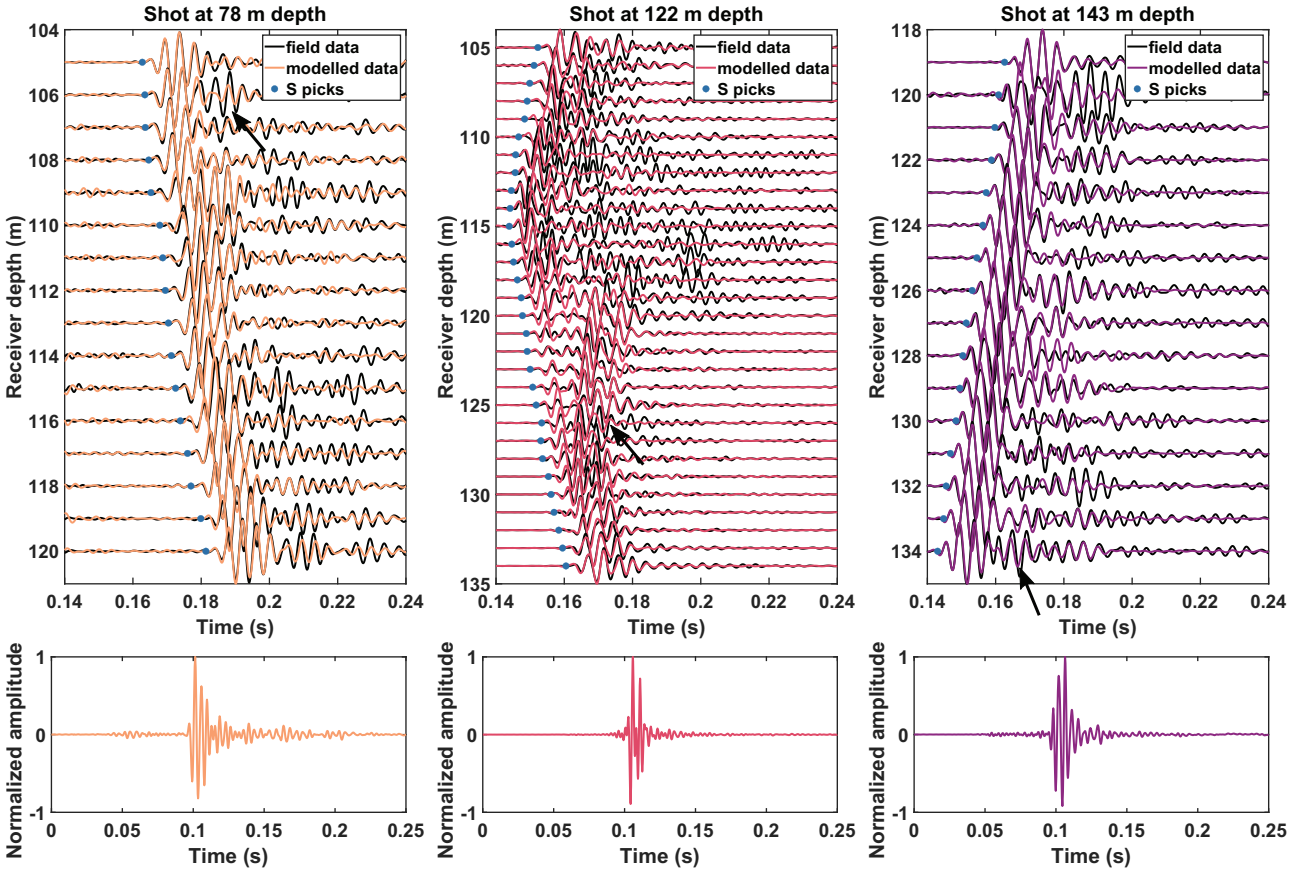

FIGURE 11 Top: SV-waveform fit for the model at stage 6 (80–350 Hz) of the FWI (Figure 8 (bottom)) with the traveltime tomography models in Figure 5 used as starting models. The arrows mark where we observed a better fit at stage 4 than at stage 6. Bottom: Normalized wavelets obtained by STF inversion using the stabilized Wiener deconvolution.

Extrapolating the correlation to the 2D inversion plane, it can be observed that the high-velocity layer at the bottom (f) is related to the massive, matrix-supported and poorly sorted diamict (Dmm) found in the core. The model also exhibits a peak at x = 24 m, which could be interpreted as a moraine deposited atop the diamict by the glacier advancing from the west. The alternating high- and low-velocity layers close to borehole C in the east (e) at about 119–137 m depth nicely depict the laminated fines (Flr, Flr(d)) found in the core. These fines were interpreted by Schuster et al. (2024) as having been deposited in a proglacial lake. The depression (Figure 8 (c)) likely consists of massive, fine-grained deposits (Fm) and partly laminated sand (Sl). It may have resulted from either gravitational slumping of the sediments on the depositional slopes of the basin or from the glacier's load during an advance, which is proposed by Schuster et al. (2024), and was later refilled. More evidence for the glacial advance is provided by the about 2 m thick layer of very low SV-wave velocity at about 119 m depth, where Schuster et al. (2024) distinguish between two lithofacies assemblages. Although the change in velocity is small, it indicates above-average consolidation by the glacier that has increased the density and reduced the SV-wave velocity at the constant shear strength of the material which was measured with a vane-shear tester in the core (Schuster et al., 2024). Anselmetti et al. (2010), O'Regan et al. (2010) and Dehnert et al. (2012) interpret this as an indicator of compaction from ice contact, again suggesting a glacial advance. The high-velocity layers observed on the receiver side at about 114 m depth (Figure 7b) are associated with the sand that is identified in the core as horizontally bedded sand (Sh) and attributed to hyper-concentrated density flow deposits (Mulder & Alexander, 2001) and the filling of subaqueous channels (Sh). Finally, the high-velocity layer at approximately 107 m depth coincides with mud-clasts found in the core.

DISCUSSION

We invert the SV-wave velocity distribution in a dense transmission geometry, which predominantly samples the medium along horizontal ray paths with a source and receiver spacing of 1 m. Furthermore, the high frequencies, excited by the source, are preserved in the data by the crosshole

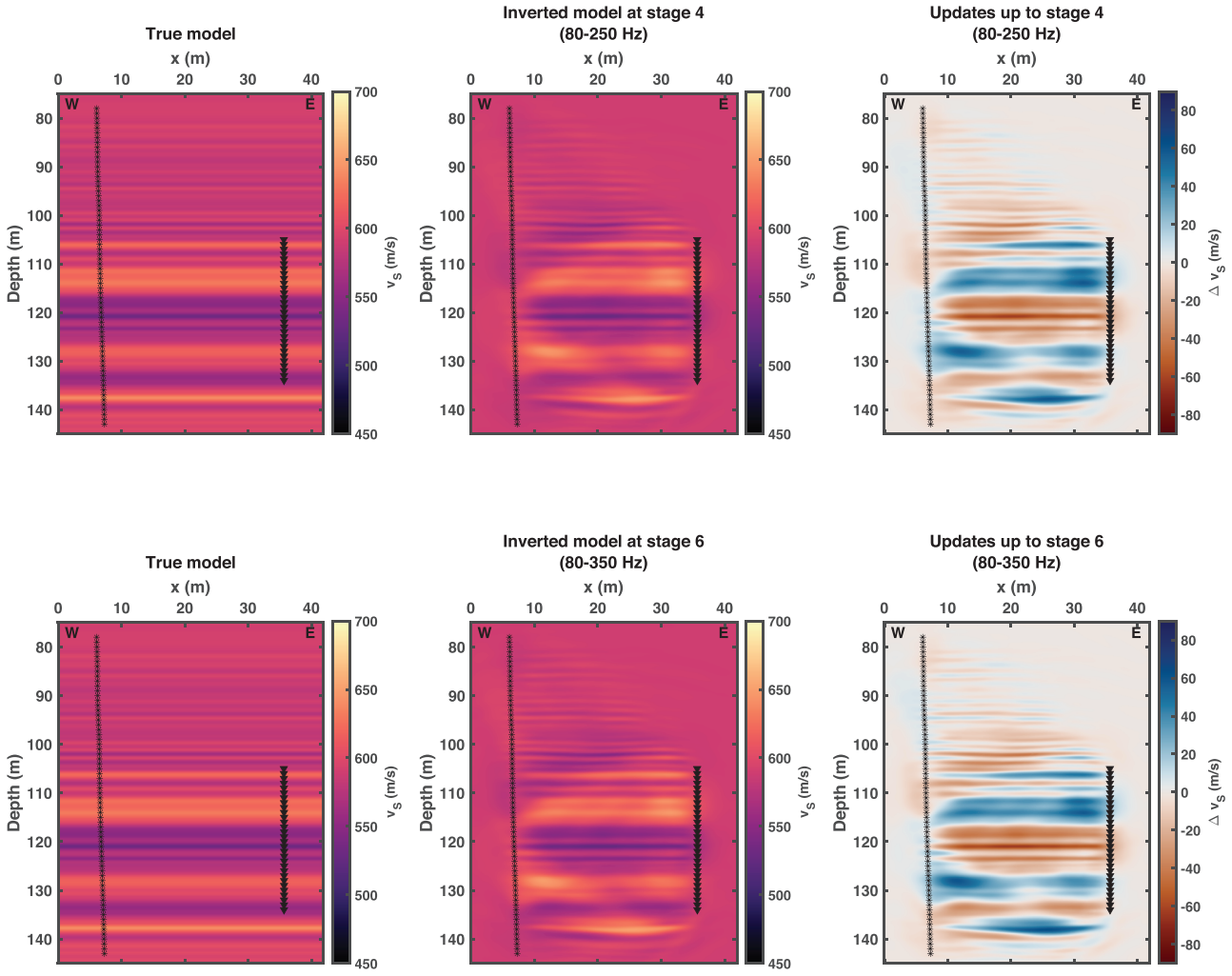

FIGURE 12 Synthetic resolution test using a 1D layered model. Source positions are marked by stars (*), and receiver positions are marked by triangles (▼). Left: True model, centre: inverted model at stage 4 (top) and stage 6 (bottom) using a homogeneous starting model and right: the difference between the initial and inverted model at stage 4 (top) and stage 6 (bottom). In regions of good wavefield coverage layers of about 1 m thickness can be recovered.

configuration situated below the attenuating weathering layer, resulting in a peak frequency of the SV-wave up to 350 Hz (Figure 3). While the high source frequencies promise high-resolution images, it would be beneficial to adapt them to the target in terms of given borehole distance, desired resolution, and site-specific attenuation, thus avoiding the time-consuming process of transmitting finely sampled data.

As shown in Figure 5, the P-wave and the SV-wave tomography models are structurally different. Where the SV-wave velocity model resolves a high-velocity depression at intermediate depth, the P-wave velocity model indicates a horizontally layered medium with velocity variations from west to east. From the structural differences, we infer an inconsistent spatial distribution of the bulk modulus that is additionally contained in the P-wave velocity and the shear modulus. Concerning the material parameters, we also expect that the density estimated based on the SV-wave velocity will introduce a bias into the subsequent FWI. The necessity to correct the SV-wave velocity model by -5% can be explained by systematically too early picks at the frequency range considered for FWI. This indicates the presence of a visco-elastic medium, where the phase velocity is smaller at low than at high frequencies according to Futterman (1962), which is called velocity dispersion.

Our FWI strategy using the tomography models leads to a relatively quick convergence of the FWI with less than 130 iterations, despite the high frequencies and the resulting fine FD discretization. Computationally, we reduce the amount of resources required by using an optimal FD discretization, domain decomposition and shot parallelization to run the isotropic, time domain, high-frequency FWI in about 2 days on a high-performance computer cluster using 128 cores and 5 GB RAM in total. In addition, we take advantage of a reduced Nyquist criterion suggested by Kurzmann (2012) to

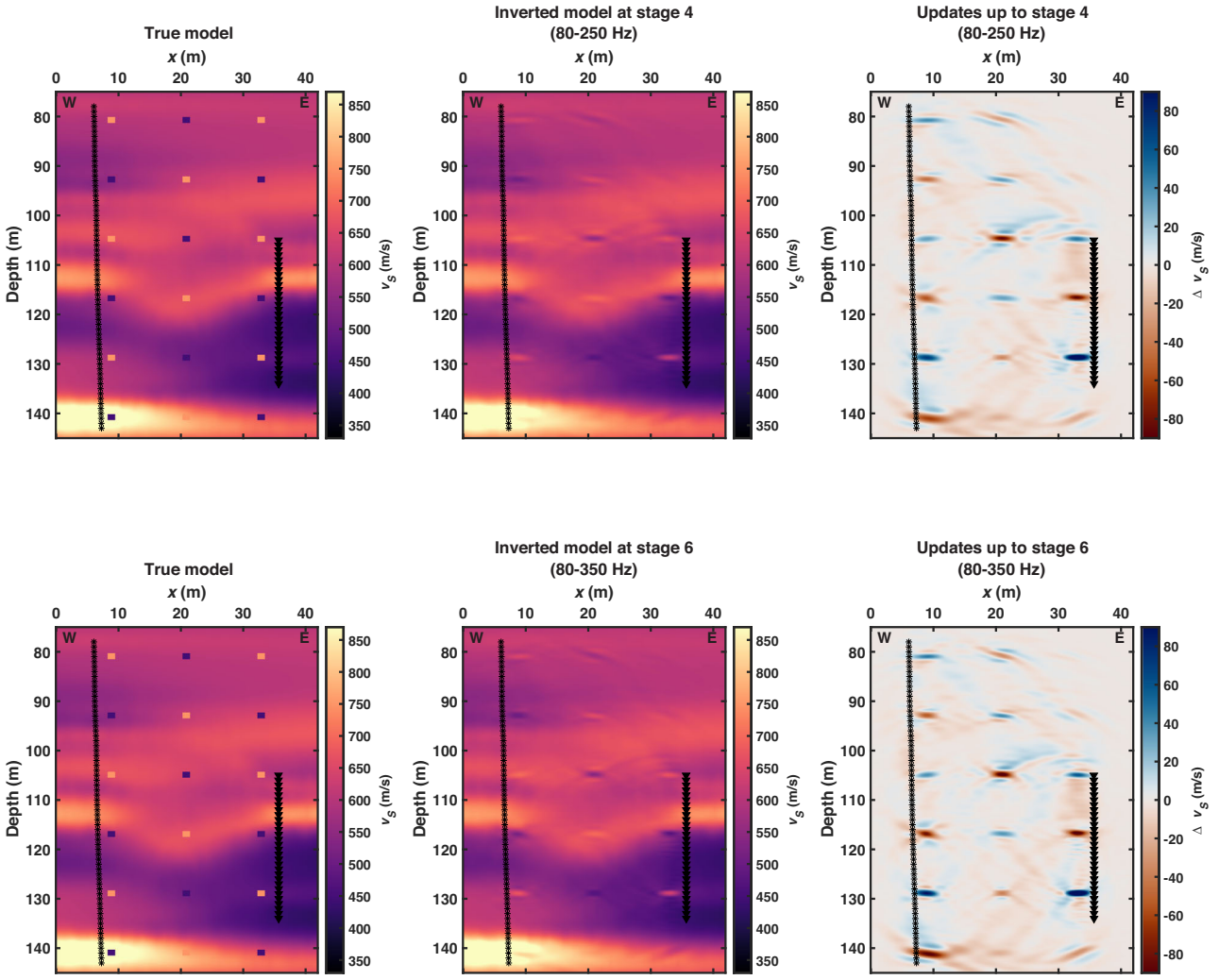

FIGURE 13 Synthetic resolution test using the traveltime tomography models including low- and high-velocity anomalies. Source positions are marked by stars (*), and receiver positions are marked by triangles (▼). Left: True model, centre: inverted model at stage 4 (top) and at stage 6 (bottom) and right: the difference between the initial and inverted model at stage 4 (top) and stage 6 (bottom). In regions of good wavefield coverage and large velocity contrasts relative to the background model, the anomalies can be recovered well. At frequencies up to 350 Hz (stage 6), the anomalies are sharpest.

reduce the number of forward modelled wavefields that need to be stored for gradient computation. The l-BFGS method also helps to reduce the sensitivity to the initial model (Zhang et al., 2012).

We consider the stage 4 FWI results as a good compromise between the waveform fit (Figure 11) and the occurrence of small-scale structures in the model. The remaining amplitude misfits of later arrivals might be related to the global correlation norm that was chosen as a misfit function. This primarily leads to a phase adjustment and gives a lower weight to the amplitudes, in order to mitigate the source–receiver coupling effects that are deemed critical for this dataset. Alternatively, the waveform misfits might indicate a contribution from 3D effects in the field data at higher frequencies. Despite the application of a 2D-to-3D spreading correction in the pre-processing of the data (subsection 4.2), which accounts for the phase and amplitude changes caused by the 2D modelling, the 3D geological information arriving from the first-order Fresnel volume with a width of about 6.0–13.2 m at 250 Hz remains in the data and cannot be fitted in the inversion. This may also cause some artefacts in the inverted model, particularly at higher frequencies where seismic waves are capable of detecting small-scale heterogeneities within the medium, which might be indicated by the waveform fit at stage 6 (Figure 11). A further reduction of the amplitude misfit might be achieved by a visco-elastic FWI. In addition, the finely layered sediments (Figure 8 (e)) can be expected to be seismically anisotropic, such that both an anisotropic traveltime tomography and FWI might yield an even better data fit and more accurate description of the physical subsurface conditions. Neglecting the anisotropy leads to distortions. Anisotropic parameter models, however, often suffer

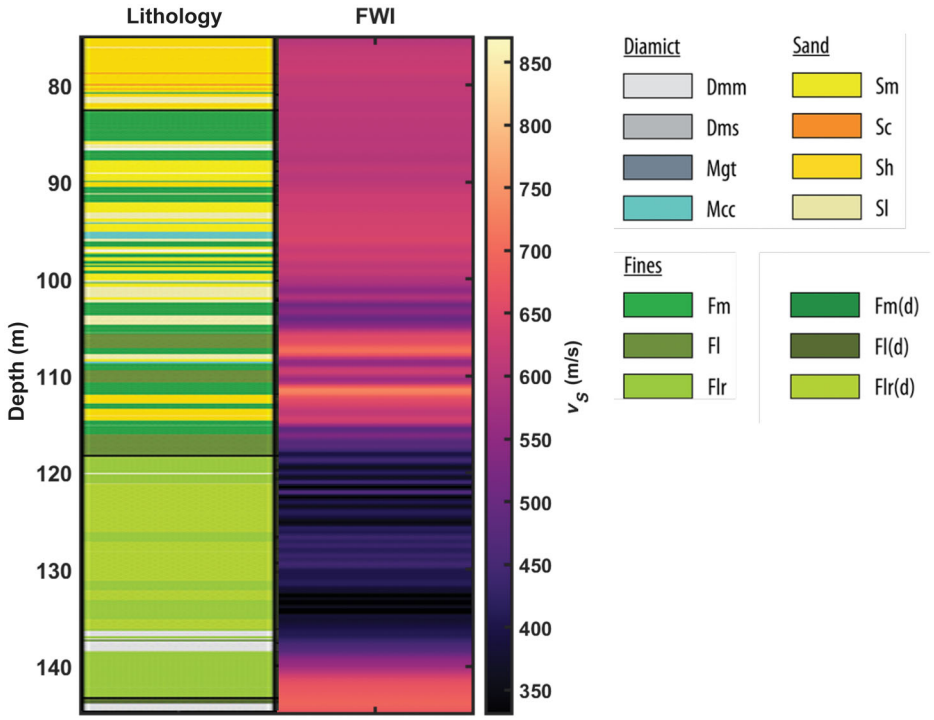

FIGURE 14 SV-wave velocity profiles extracted from the FWI result at stage 4 along borehole C compared to final lithology (modified after Schuster et al. (2024)).

from parameter trade-off as shown by a synthetic study by Kazei & Alkhalifah 2019 and a field data study by Manukyan and Maurer (2020). Furthermore, the angular coverage of our crosshole experiment is too restricted to properly characterize the anisotropy and derive reliable anisotropy parameters. To increase the angular coverage, a longer receiver string with more stations would have been required. This elongation of the receiver spread could also be achieved by deploying a distributed acoustic sensing cable, which was tested by Koedel et al. (2024).

Although the computational effort of FWI is much larger than that of traveltime tomography, it is well justified by the achieved increase of resolution. Both resolution tests do not indicate significant kernel artefacts and show that structures can only be resolved in the regions of dense wavefield coverage, as marked in Figure 2. The enhanced resolution capability at the receiver side can be ascribed to the denser wavefield coverage and the cylindrical source tapers following an error function with a radius of 0.5 m which are applied in the inversion and yield a smoothing effect around the source positions. The 1D resolution test, which closely resembles the subsurface structures expected and observed in area (e) (Figure 8), also does not show small-scale, bend structures suggesting that those are not artefacts in the common sense. Instead, we hypothesize that those structures are related to reflection information contained in the higher Fresnel zones and the additional, oval migration isochrones (Mora, 1989; Yao et al., 2020), which causes the FWI to produce model updates that look similar to the impedance contrasts obtained by waveform imaging at the frequencies added at stage 4 of the FWI. At the same time, small-scale structures are introduced by the higher frequencies, which are investigated by the second resolution test. The checkerboard test reveals the horizontal resolution capability which is linked to the horizontal length of the anisotropic gradient smoothing operator. This results in a notable smoothing effect in the horizontal direction, while it simultaneously sharpens vertical velocity contrasts originating from layer boundaries.

This improvement in vertical resolution subsequently allows us to compare individual layers, with a thickness close to 1 m, in the SV-wave velocity model and the core data of borehole C. The correlation with the lithology within the limits of vertical resolution in the FWI and the depth error of, on average, ±0.2 m of sources and receivers is highly satisfactory. The observation that the diamict layer just above 140 m cannot be identified in the velocity profile, is attributed to an inadequate wavefield coverage. In addition, the thick and significantly denser diamict layer situated below 140 m (Schuster et al., 2024) will act as a strong reflector and will result in a superposition of the transmitted wave and the reflections that arrive almost simultaneously at the receivers, given the longer coda characteristic of the inverted source wavelets. Therefore, we expect and can identify a strong smearing effect of the velocity distribution at depths below the first diamict layer.

CONCLUSIONS

Our study presents an innovative field data application of FWI in the complex geological environment of a glacially overdeepened basin using SV-waves. The result demonstrates that the dense crosshole setup allows to obtain a high-resolution subsurface SV-wave velocity model using elastic isotropic time-domain FWI. It is also evident that we reach the frequency regime in which the FWI result shows similarity with seismic imaging. The inverted model reflects this by introducing small-scale structures, which allows us to distinguish layers of 1 m thickness and structures that look like impedance contrasts. The model is validated along the receiver borehole trajectory for the range of the source depths by correlation with the core data, thereby providing further evidence for an additional glacial advance proposed to be identified at 119 m. In addition, the model shows a laterally heterogeneous medium that cannot be mapped by either the core or wireline logging. Thus, the model provides two-dimensional information on the shear properties. This information about the subsurface cannot be obtained by acoustic FWI but is important for geotechnical site investigations. An example is the determination of elastic soil properties for the purpose of site classification and the application of building codes. The latter are defined based on site amplification effects of earthquakes and consider the impact of the load of buildings.

ACKNOWLEDGEMENTS

We thank the Deutsche Forschungsgemeinschaft (grants: BU 3894/2-1, BU 2467/3-1 and KO 6375/1-1) for funding the seismic crosshole experiments within the priority program 1006 (ICDP/IODP). We acknowledge the International Continental Drilling Program (ICDP) for their continued support and funding for the drilling of the three boreholes at ICDP site 5068_1. The seismic crosshole equipment was rented from Geotomographie GmbH, Neuwied, Germany. A special thanks to the technical staff of LIAG-FA1.1 Jan Bayerle, Sven Wedig and Jan Bergmann Barrocas as well as our student assistant Kim Ripke for their vigorous support in the field. Furthermore, we thank Vladimir Kazei, Shibo Xu, the associated editor Carlos Calderón-Macías, as well as the editor Alireza Malehmir, for their very helpful and constructive comments, which significantly improved the quality of the paper. Additional thanks go to the Applied Geophysics working group at KIT for helpful discussions about FWI and the DOVE group for valuable insights into the geology of overdeepened basins. Pre-processing of the data was done using an academic license of Shearwater's Reveal software and the open-source code BIRGIT. FWI was performed on the NEC-HPC Linux Cluster at Kiel University using the DENISE-Black Edition code.

Open access funding enabled and organized by Projekt DEAL.

DATA AVAILABILITY STATEMENT

Upon completion of the project, the seismic data will be accessible via GFZ data services (https://doi.org/10.5880/ICDP.5068.002; Beraus et al., 2024).

ORCID

Sarah Beraus https://orcid.org/0009-0000-6984-3098

REFERENCES

Anselmetti, F.S., Drescher-Schneider, R., Furrer, H., Graf, H.R., Lowick, S.E., Preusser, F. & Riedi, M.A. (2010) A ~180,000 years sedimentation history of a perialpine overdeepened glacial trough (Wehntal, N-Switzerland). *Swiss Journal of Geosciences*, 103(3), 345–361.

Bauer, K., Pratt, R., Weber, M., Haberland, C., Ryberg, T., Medioli, B. & Shimizu, S. (2003) Crosswell seismic studies in Gas Hydrate-bearing sediments: P wave velocity and attenuation tomography. *EGS - AGU - EUG Joint Assembly*. https://ui.adsabs.harvard.edu/abs/2003EAEJA....12377B

Bauer, K., Pratt, F., Weber, M., Ryberg, T., Haberland, C. & Shimizu, S. (2005) Mallik 2002 cross-well seismic experiment: project design, data acquisition, and modelling studies. in: *Scientific Results from the Mallik 2002 Gas Hydrate Production Research Well Program*, Mackenzie Delta, Northwest Territories, Canada, edited by: Dallimore, S. R. and Collett, T. S., vol. 585 of GSC Bulletin, Geological Survey of Canada, 14 pp., ISBN 978-0-66019339-7, 2005.

Beraus, S., Buness, H., Bayerle, J., Bergmann Barrocas, J., Wedig, S., Ripke, K. et al. (2024) Crosshole seismic data at ICDP site 5068_1. https://dataservices.gfz-potsdam.de/icdp/showshort.php?id=9621d62a-5ef1-11ef-967a-4ffbfe06208e

Beraus, S., Burschil, T., Buness, H., Köhn, D., Bohlen, T. & Gabriel, G. (2024) A comprehensive crosshole seismic experiment in glacial sediments at the ICDP DOVE site in the Tannwald Basin. *Scientific Drilling*, 33(2), 237–248. https://sd.copernicus.org/articles/33/237/2024/

Bleistein, N. (1986) Two-and-one-half dimensional in-plane wave propagation. *Geophysical Prospecting*, 34(5), 686–703. https://onlinelibrary.wiley.com/doi/pdf/10.1111/j.1365-2478.1986.tb00488.x.

Buness, H., Tanner, D.C., Burschil, T., Gabriel, G. & Wielandt-Schuster, U. (2022) Cuspate-lobate folding in glacial sediments revealed by a small-scale 3-D seismic survey. *Journal of Applied Geophysics*, 200, 104614.

Bunks, C., Saleck, F., Zaleski, S. & Chavent, G. (1995) Multiscale seismic wave-form inversion. *Geophysics*, 60, 1457–1473.

Burschil, T., Buness, H., Tanner, D., Wielandt-Schuster, U., Ellwanger, D. & Gabriel, G. (2018) Highresolution reflection seismics reveal the structure and the evolution of the Quaternary glacial Tannwald Basin. *Near Surface Geophysics*, 16, 593–610.

Buske, S., Lecomte, I., Nemeth, T., Operto, S. & Sallares, V. (2009) Imaging and inversion – Introduction. *Geophysics*, 74, WCA1–WCA4.

Choi, Y. & Alkhalifah, T. (2012) Application of multi-source waveform inversion to marine streamer data using the global correlation norm. *Geophysical Prospecting*, 60(4), 748–758. https://onlinelibrary.wiley.com/doi/pdf/10.1111/j.1365-2478.2012.01079.x.

Cook, S. & Swift, D. (2012) Subglacial basins: their origin and importance in glacial systems and landscapes. *Earth-Science Reviews*, 115, 332–372.

Courant, R., Friedrichs, K. & Lewy, H. (1967) On the partial difference equations of mathematical physics. *IBM Journal of Research and Development*, 11(2), 215–234.

Dablain, M.A. (1986) The application of highorder differencing to the scalar wave equation. *Geophysics*, 51(1), 54–66.

Dehnert, A., Lowick, S.E., Preusser, F., Anselmetti, F.S., Drescher-Schneider, R., Graf, H.R., Heller, F., Horstmeyer, H., Kemna, H.A., Nowaczyk, N.R., Züger, A. & Furrer, H. (2012) Evolution of an overdeepened trough in the northern Alpine Foreland at Niederweningen, Switzerland. *Quaternary Science Reviews*, 34, 127–145.

Dokter, E., Köhn, D., Wilken, D., De Nil, D. & Rabbel, W. (2017) Full waveform inversion of SH- and Love-wave data in near-surface prospecting. *Geophysical Prospecting*, 65(S1), 216–236. https://onlinelibrary.wiley.com/doi/pdf/10.1111/1365-2478.12549.

Ellwanger, D., Lämmermann-Barthel, J. & Neeb, I. (2003) Eine landschaftsübergreifende Lockergesteinsgliederung vom Alpenrand zum Oberrhein. *GeoArchaeoRhein*, 4, 81–124.

Ellwanger, D., Wielandt-Schuster, U., Franz, M. & Simon, T. (2011) The Quaternary of the southwest German Alpine Foreland (Bodensee, Oberschwaben, Baden- Württemberg, Southwest Germany). *Quaternary Science Journal 0424-7116*, 60, 306–328.

Fichtner, A. (2011) *Full seismic waveform modelling and inversion*. Cham: Springer.

Forbriger, T., Groos, L. & Schäfer, M. (2014) Line-source simulation for shallow-seismic data. Part 1: theoretical background. *Geophysical Journal International*, 198(3), 1387–1404.

Futterman, W.I. (1962) Dispersive body waves. *Journal of Geophysical Research (1896-1977)*, 67(13), 5279–5291. https://onlinelibrary.wiley.com/doi/abs/10.1029/JZ067i013p05279

Gallardo, L.A. & Meju, M.A. (2004) Joint two-dimensional DC resistivity and seismic travel time inversion with cross-gradients constraints. *Journal of Geophysical Research: Solid Earth*, 109(B3), B03311. https://onlinelibrary.wiley.com/doi/pdf/10.1029/2003JB002716.

Gao, L., Pan, Y., Rieder, A., Bohlen, T. & Mao, W. (2023) Multiparameter 2-D viscoelastic full-waveform inversion of Rayleigh waves: a field experiment at Krauthausen test site. *Geophysical Journal International*, 234(1), 297–312.

Gaucher, E., Azzola, J., Schulz, I., Meinecke, M., Dirner, S., Steiner, U. & Thiemann, K. (2020) Active cross-well survey at geothermal site Schäftlarnstraße. Researchgate, https://www.researchgate.net/publication/348232434_Active_cross-well_survey_at_geothermal_site_Schaftlarnstrasse

Gegg, L. & Preusser, F. (2023) Comparison of overdeepened structures in formerly glaciated areas of the northern Alpine foreland and northern central Europe. *E&G Quaternary Science Journal*, 72(1), 23–36.

Günther, T., Rücker, C. & Spitzer, K. (2006) Three-dimensional modelling and inversion of DC resistivity data incorporating topography II. Inversion. *Geophysical Journal International*, 166(2), 506–517.

Groos, L., Schäfer, M., Forbriger, T. & Bohlen, T. (2017) Application of a complete workflow for 2D elastic full-waveform inversion to recorded shallow-seismic Rayleigh waves. *Geophysics*, 82(2), R109–R117.

Hadden, S., Pratt, R.G. & Smithyman, B. (2019) Anisotropic full-waveform inversion of crosshole seismic data: a vertical symmetry axis field data application. *Geophysics*, 84(1), B15–B32.

Jordi, C., Doetsch, J., Günther, T., Schmelzbach, C. & Robertsson, J.O. (2018) Geostatistical regularization operators for geophysical inverse problems on irregular meshes. *Geophysical Journal International*, 213(2), 1374–1386.

Kazei, V. & Alkhalifah, T. (2019). Scattering radiation pattern atlas: What anisotropic elastic properties can body waves resolve? *Journal of Geophysical Research: Solid Earth*, 124, 2781–2811. https://doi.org/10.1029/2018JB016687

Koedel, U., Stork, A.L., David, A. & Fechner, T. (2024) Evaluating distributed acoustic sensing for crosswell seismic surveys with helical and linear fibers using conventional P-, SH-, and SV-wave sources. *The Leading Edge*, 43(11), 726–734. https://doi.org/10.1190/tle43110726.1

Köhn, D., De Nil, D., Kurzmann, A., Przebindowska, A. & Bohlen, T. (2012) On the influence of model parametrization in elastic full waveform tomography. *Geophysical Journal International*, 191(1), 325–345. https://onlinelibrary.wiley.com/doi/pdf/10.1111/j.1365-246X.2012.05633.x.

Köhn, D., Wilken, D., De Nil, D., Wunderlich, T., Rabbel, W., Werther, L., Schmidt, J., Zielhofer, C. & Linzen, S. (2019) Comparison of time-domain SH waveform inversion strategies based on sequential low and bandpass filtered data for improved resolution in near-surface prospecting, *Journal of Applied Geophysics*, 160, 69–83.

Komatitsch, D. & Martin, R. (2007) An unsplit convolutional Perfectly Matched Layer improved at grazing incidence for the seismic wave equation. *Geophysics*, 72, SM155–SM167.

Kurzmann, A. (2012) *Applications of 2D and 3D full waveform tomography in acoustic and viscoacoustic complex media*. PhD Thesis, Karlsruher Institut für Technologie (KIT).

Lazaratos, S.K., Harris, J.M., Rector, J.W. & Van Schaack, M. (1995) High-resolution crosswell imaging of a West Texas carbonate reservoir; Part 4, Reflection imaging. *Geophysics*, 60(3), 702–711.

Levander, A. (1988) Fourth-order finite-difference P-S. *Geophysics*, 53, 1425–1436.

Manukyan, E. & Maurer, H. (2020) Elastic vertically transversely isotropic full-waveform inversion using cross-gradient constraints an application toward high-level radioactive waste repository monitoring. *Geophysics*, 85(4), R313–R323. https://doi.org/10.1190/geo2019-0061.1

McMechan, G.A. (1983) Seismic tomography in boreholes. *Geophysical Journal of the Royal Astronomical Society*, 74(2), 601–612. https://onlinelibrary.wiley.com/doi/pdf/10.1111/j.1365-246X.1983.tb01891.x.

Mecking, R., Köhn, D., Meinecke, M. & Rabbel, W. (2021) Cavity detection by SH-wave full-waveform inversion: a reflection-focused approach. *Geophysics*, 86(3), WA123–WA137.

Mora, P. (1989) Inversion = migration + tomography. *Geophysics*, 54(12), 1575–1586. https://doi.org/10.1190/1.1442625

Métivier, L. & Brossier, R. (2016) The SEISCOPE optimization toolbox: a large-scale nonlinear optimization library based on reverse communication. *Geophysics*, 81(2), F1–F15.

Mulder, T. & Alexander, J. (2001) The physical character of subaqueous sedimentary density flows and their deposits. *Sedimentology*, 48(2), 269–299. https://onlinelibrary.wiley.com/doi/pdf/10.1046/j.1365-3091.2001.00360.x.

Nocedal, J. & Wright, S. (2006) *Numerical optimization*. Cham: Springer.

O'Regan, M., Jakobsson, M. & Kirchner, N. (2010) Glacial geological implications of overconsolidated sediments on the Lomonosov Ridge and Yermak Plateau. *Quaternary Science Reviews*, 29(25), 3532–3544.

Pfiffner, O. (2014) *Geology of the Alps*. Oxford, UK: Wiley-Blackwell.

Pfiffner, O.A. (1986) Evolution of the North Alpine Foreland Basin in the Central Alps. In *Foreland basins*. New York: John Wiley & Sons, pp. 219–228. https://onlinelibrary.wiley.com/doi/pdf/10.1002/9781444303810.ch11.

Plessix, R.-E. (2008) Introduction: towards a full waveform inversion. *Geophysical Prospecting*, 56(6), 761–763. https://onlinelibrary.wiley.com/doi/pdf/10.1111/j.1365-2478.2008.00736.x.

Pratt, R., Hou, F., Bauer, K. & Weber, M. (2005) Waveform tomography images of velocity and inelastic attenuation from the Mallik 2002 crosshole seismic surveys. in: *Scientific Results from the Mallik 2002 Gas Hydrate Production Research Well Program*, Mackenzie Delta, Northwest Territories, Canada,.edited by: Dallimore, S. R. and Collett, T. S., vol. 585 of GSC Bulletin, Geological Survey of Canada, 122 pp., ISBN 978-0-66019339-7, 2005.

Pratt, R. & Shipp, R. (1999) Seismic waveform inversion in the frequency domain, Part 2: Fault delineation in sediments using crosshole data. *Geophysics*, 64(3), 902–914.

Preusser, F., Reitner, J.M. & Schlüchter, C. (2010) Distribution, geometry, age and origin of overdeepened valleys and basins in the Alps and their foreland. *Swiss Journal of Geosciences*, 103(3), 407–426.

Rao, Y. & Wang, Y. (2005) Crosshole seismic tomography: working solutions to issues in real data travel time inversion. *Journal of Geophysics and Engineering*, 2(2), 139–146.

Rao, Y., Wang, Y. & Morgan, J. (2006) Crosshole seismic waveform tomography II. Resolution analysis. *Geophysical Journal International*, 166, 1237–1248.

Ravaut, C., Operto, S., Improta, L., Virieux, J., Herrero, A. & DellAversana, P. (2004) Multiscale imaging of complex structures from multifold wide-aperture seismic data by frequency-domain full-waveform tomography: application to a thrust belt. *Geophysical Journal International*, 159, 1032–1056.

Rector, J.W., Lazaratos, S.K., Harris, J.M. & Van Schaack, M. (1995) High-resolution crosswell imaging of a West Texas carbonate reservoir; Part 3, Wavefield separation of reflections. *Geophysics*, 60(3), 692–701.

Rücker, C., Günther, T. & Wagner, F.M. (2017) pyGIMLi: an open-source library for modelling and inversion in geophysics. *Computers and Geosciences*, 109, 106–123.

Schäfer, M., Groos, L., Forbriger, T. & Bohlen, T. (2014) Line-source simulation for shallow-seismic data. Part 2: full-waveform inversion: a synthetic 2-D case study. *Geophysical Journal International*, 198(3), 1405–1418.

Schuster, B., Gegg, L., Schaller, S., Buechi, M.W., Tanner, D.C., Wielandt-Schuster, U., Anselmetti, F.S. & Preusser, F. (2024) Shaped and filled by the rhine glacier: the overdeepened Tannwald Basin in Southwestern Germany. *Scientific Drilling*, 33, 191–206.

Schwardt, M., Köhn, D., Wunderlich, T., Wilken, D., Seeliger, M., Schmidts, T., Brückner, H., Başaran, S. & Rabbel, W. (2020) Characterization of silty to fine-sandy sediments with SH waves: full waveform inversion in comparison with other geophysical methods. *Near Surface Geophysics*, 18(3), 217–248. https://onlinelibrary.wiley.com/doi/pdf/10.1002/nsg.12097.

Singh, S., Tsvankin, I. & Naeini, E.Z. (2021) Facies-based full-waveform inversion for anisotropic media: a North Sea case study. *Geophysical Prospecting*, 69(8-9), 1650–1663. https://onlinelibrary.wiley.com/doi/pdf/10.1111/1365-2478.13139.

Singh, S., Tsvankin, I. & Zabihi Naeini, E. (2020) Full-waveform inversion with borehole constraints for elastic VTI media. *Geophysics*, 85(6), R553–R563.

Stümpel, H., Kähler, S., Meissner, R. & Milkereit, B. (1984) The use of seismic shear waves and compressional waves for lithological problems of shallow sediments. *Geophysical Prospecting*, 32(4), 662–675. https://onlinelibrary.wiley.com/doi/pdf/10.1111/j.1365-2478.1984.tb01712.x.

Tarantola, A. (2005) *Inverse problem theory and methods for model parameter estimation*. Philadelphia, PA: SIAM.

Van Schaack, M., Harris, J.M., Rector, J.W. & Lazaratos, S. (1995) High-resolution crosswell imaging of a West Texas carbonate reservoir; Part 2, Wavefield modeling and analysis. *Geophysics*, 60(3), 682–691.

Virieux, J. (1984) P-SV wave propagation in heterogeneous media: velocity-stress finite-difference method. *Geophysics*, 51, 889–901.

Virieux, J. & Operto, S. (2009) An overview of full-waveform inversion in exploration geophysics. *Geophysics*, 74(6), WCC1–WCC26.

von Ketelhodt, J., Fechner, T., Manzi, M. & Durrheim, R. (2018) Joint-inversion of cross-borehole P-waves, horizontally and vertically polarised S-waves: tomographic data for hydrogeophysical site characterisation. *Near Surface Geophysics*, 16, 529–542.

Wang, Y. & Rao, Y. (2006) Crosshole seismic waveform tomography I. Strategy for real data application. *Geophysical Journal International*, 166(3), 1224–1236. https://onlinelibrary.wiley.com/doi/pdf/10.1111/j.1365-246X.2006.03030.x.

Yao, G., Wu, D. & Wang, S.X. (2020) A review on reflection-waveform inversion. *Petroleum Science*, 17(2), 334–351. https://doi.org/10.1007/s12182-020-00431-3

Zhang, F., Juhlin, C., Cosma, C., Tryggvason, A. & Pratt, R.G. (2012) Cross-well seismic waveform tomography for monitoring CO_2 injection: a case study from the Ketzin Site, Germany. *Geophysical Journal International*, 189(1), 629–646. https://onlinelibrary.wiley.com/doi/pdf/10.1111/j.1365-246X.2012.05375.x.

Zhou, C., Schuster, G.T., Hassanzadeh, S. & Harris, J.M. (1997) Elastic wave equation traveltime and waveform inversion of crosswell data. *Geophysics*, 62(3), 853–868.

How to cite this article: Beraus, S., Köhn, D., Bohlen, T., Burschil, T., Schuster, B., Buness, H. et al. (2025) Seismic crosshole full-waveform inversion of high-frequency SV-waves for glacial sediment characterization. *Geophysical Prospecting*, 73, 1587–1605. https://doi.org/10.1111/1365-2478.70024

APPENDIX A: TRAVELTIME TOMOGRAPHY PARAMETERS

TABLE A.1 Traveltime tomography parameters for the separate inversion of the P- and SV-wave first arrival picks. We use an unstructured triangular mesh. The quality parameter refers to the minimum angle permitted in a triangle. The area parameter defines the cell size. The starting models are provided in terms of slowness, denoted as p_0, which is inversely proportional to velocity. The data error is given as the estimated sum of position and picking error. The damping parameter λ is chosen such that there is a minimum systematic data residual by the end of the inversion, given that the L-curve did not allow the determination of an optimal damping parameter. The parameters L_x and L_z define the length of the horizontal and vertical axes of the geostatistical regularization ellipse, respectively. The last parameter gives the number of secondary nodes employed in the ray tracing scheme used to forward model the data.

Wavetype	Mesh	Quality	Area (m^2)	p_0 (s/m)	Data error (ms)	λ	L_x (m)	L_z (m)	Number of secondary nodes
P	Triangular	34	2	1/1770	0.125	2000	50	2	5
SV	Triangular	34	2	1/590	0.5	200	30	2	3